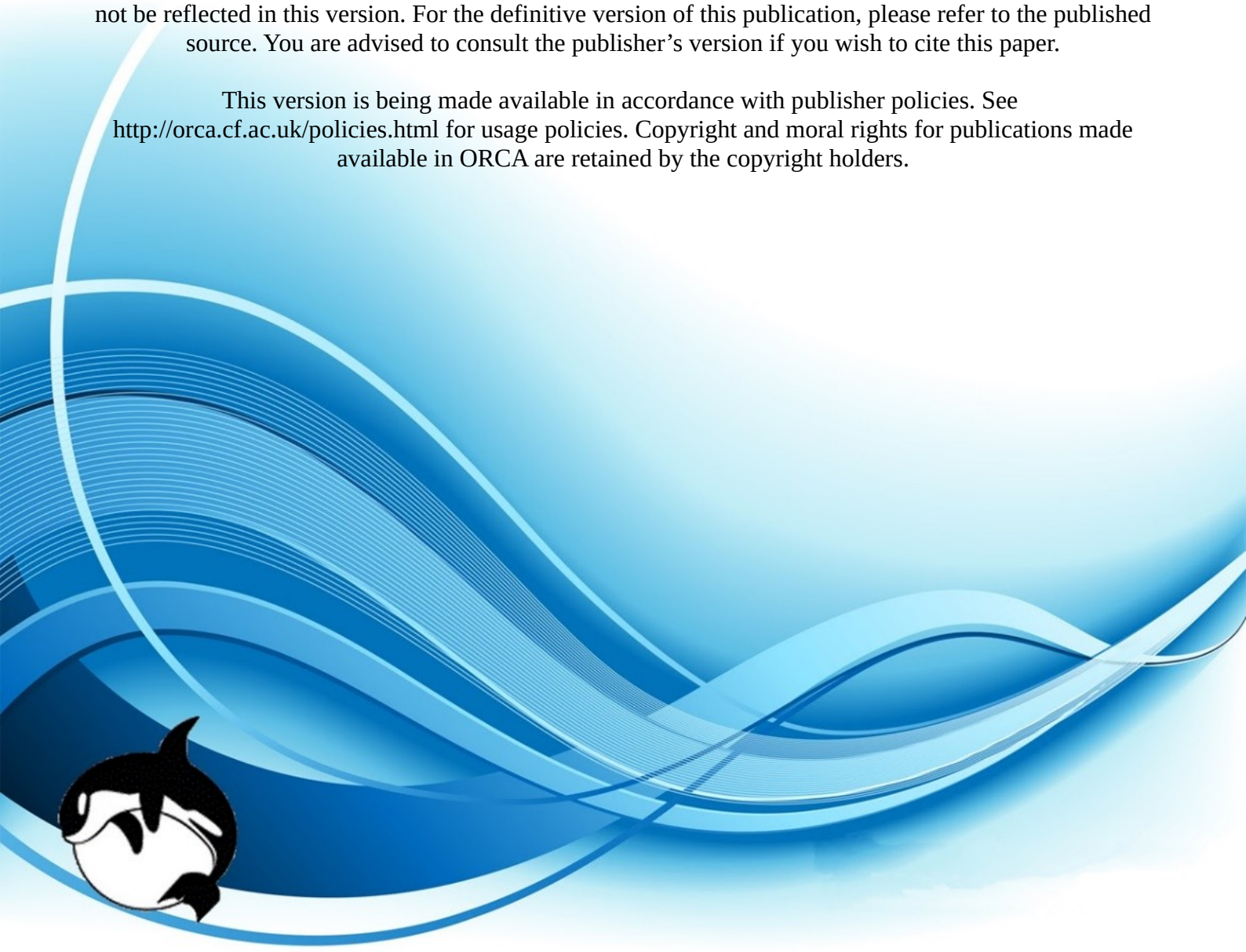

Highly-efficient electro-optically tunable smart-supercapacitor using an oxygen-excess nanograin tungsten oxide thin film

Akbar I. Inamdar[1], Jongmin Kim[1], Yongcheol Jo[1], Hyeonseok Woo[1], Sangeun Cho[1], Sambhaji M. Pawar[1], Yuljae Cho[2], Bo Hou[2], SeungNam Cha[2], Jungwon Kwak[3], Hyungsang Kim[1], and Hyunsik Im[1,*]

[1]Division of Physics and Semiconductor Science, Dongguk University, Seoul 100-715, South Korea

[2]Department of Engineering Science, University of Oxford, Parks Road, OX1 3PJ, UK

[3]Medical Physics Department, Asan Medical Center, Seoul, South Korea

Next-generation electronic technology requires the use of advanced energy storage devices with integrated functionality to fulfill key application requirements. A smart supercapacitor shares the same electrochemical processes as a conventional energy storage device in addition to electrochromic functionality. It can sense the energy storage level and can display it in a noticeable manner, which results in added convenience to everyday applications. In this study we have developed a smart supercapacitor that uses tungsten oxide nanograin thin film to provide the combined advantages of energy storage and electrochromism. The nanostructured tungsten oxide is dark blue in the charged state and becomes transparent in its discharged state; and it has a specific capacitance of 228 Fg^{-1} at 0.25 Ag^{-1} with a quite large potential window of 1.4 V. It is highly durable, exhibits good electrochemical stability over 2000 cycles, retains a significant charge storage of 75%; and exhibits a high coloration efficiency of ~170 cm^2/C with an optical modulation of 82%. The smart-supercapacitor fabricated with this material exhibits a superb combination of

energy storage and electrochromic features in one device to monitor the energy storage level through visible changes in color.

Keywords: - supercapacitor, electrochromism, tungsten oxide, thin film
E-mail: hyunsik7@dongguk.edu, akbarphysics2002@gmail.com

1. Introduction

As the demand for advanced electronic devices increases, the need to develop high-performance, and multi-functional materials has also increased and this trend is also true for energy storage technology. It is inevitable to integrate greater functionality in energy storage devices in order to support the growing range of applications in portable electronics. One core example of multi-functional energy storage devices is a smart-supercapacitor, or a chromo-supercapacitor, which relies on the same electrochemical process in the electrolyte to store energy as well as to provide the electrochromic functionality [1, 2, 3, 4]. It would certainly be useful and advantageous if the user could determine the amount of energy that has been consumed while using an electronic device before the device stop working, Thus, smart supercapacitors can work as normal supercapacitor to store energy and can also sense the energy storage level through a change in the visual color (visualization of the device charge state as the degree of color saturation), and this can bring convenience to a wide range of potential applications [5, 6]. Electrochromic devices and supercapacitors rely on many common characteristics of materials, including physical and chemical operating mechanism, chemical and structural requirements.

Electrochromic supercapacitor were first studied by Wei *et al*., who used ordered bicontinuous double-gyroid vanadium pentoxide (V_2O_5) in their study [1]. They found that such devices had a specific capacitance of 155 F/g with a strong electrochromic change in color from green/gray to yellow; and they also suggested that the concept could be extended to other electrochromic compounds. $W_{18}O_{49}$/PANI composites were then found to exhibit excellent electrochemical and electrochromic behavior and to operate over a wide potential window [2]. Bilayer films made of tungsten trioxide/zinc tungstate ($WO_3/ZnWO_4$) exhibit a combined electrochromic and energy storage behavior in 0.5 M H_2SO_4 electrolyte [7].PANI/WO_3 nanocomposite films show dual electrochromism for both negative and positive potentials with a coloration efficiency of 98.4 cm^2 C^{-1} and an aerial capacitance of 0.025 Fcm^{-2} with a broader working potential window of 1.3 V [8]. On the other hand, NiO nanoparticles exhibit a large optical modulation (63.6%), a high capacitance of 1386 F/g, and a superior rate capability that shortens the ion diffusion length, facilitate charge transfer, and simultaneously monitors the energy storage level through a visual display. [3].

The challenge is to search for materials that exhibit charge storage properties and changes in color according to the charged states. Transition metal oxides (TMOs) have electrochromic coloration efficiencies along the color spectra, as illustrated in **Fig. 1,** and there are two mail kinds of electrochromic materials: cathodically and anodically coloring materials [9 -40]. Of all electrochromic TMOs, tungsten oxide (WO_3) is the most suitable for numerous applications, including electrochromism, photochromism, electrocatalysis, gas sensor, dye-sensitized solar cell and photocatalysis due to its superior properties including fast redox reaction, recognizable color changes, good chemical stability, and strong adherence to the substrate [2, 7, 8, 41]. Tungsten oxide exhibits an optical color change during intercalation/deintercalation of cations like H^+, Li^+,

Na^+ and K^+, [9-41] and it is an electrochromic material that is very sensitive to the stoichiometry and oxygen content in the film [41]. Nevertheless, to the best of our knowledge, the use of tungsten oxide in smart supercapacitors has not yet been fully explored, except for a few reports in the literature.

In this paper, we investigate the electrochromic and electrochemical supercapacitor properties of reactively-sputtered tungsten oxide nanograin thin films as a multifunctional electrodes. The highest coloration efficiency of ~170 cm^2C^{-1} and the best specific capacitance of 228 Fg^{-1} at 0.25 Ag^{-1} are achieved for the nanograin tungsten oxide thin film.

2. Experimental details

Nanograin tungsten oxide (WO3) thin film electrodes were fabricated on ITO-coated conducting glass substrates with a sheet resistance of 27 Ωcm^{-2} by using conventional radio frequency (RF) magnetron sputtering with a WO3 target (99.99% purity). The sputtering chamber was initially evacuated to 2.0×10^{-6} Torr and was then maintained at 10 mTorr with a mixture of Argon (Ar) and oxygen (O_2) gas flow. The films were grown at room temperature with an applied power of 120W and during this growth, the oxygen content of the film was determined by setting the Ar to O_2 gas ratio to 8:2 (20% oxygen). Ellipsometry was carried out to measure the average thickness of the film 138 nm. Cyclic voltammetry (CV), galvanostatic charge/discharge, and an AC impendence analysis with a potentiostat (Princeton Applied Research, VersaSTAT 3) were then carried out to determine the electrochemical characteristics of the tungsten oxide electrode. The three-electrode electrochemical cell consists of 1 M LiClO4 + PC as the electrolyte, a WO3 electrode as the working electrode, a saturated calomel electrode (SCE) as the reference electrode, and graphite as the counter-electrode. The chemical composition of the films was determined via

X-ray photoelectron spectroscopy (Ulvac-phi (Japan with X-ray beam size: 10 - 200 um) and Rutherford backscattering spectroscopy (RBS). The microstructure and grain morphology of the films were determined via transmission electron microscopy (TEM, JEOL 2010 with an Oxford EDX detector), high-resolution electron microscopy (HRTEM), and selected area electron diffraction (SAED). The acceleration voltage was set to 200 KV, and the camera length was 20 cm. The film morphology was studied using atomic force and scanning electron microscopy (FE-SEM, Model: JSM-6701F, JEOL, Japan). The crystal structure and the phase evolution were then studied using X-ray diffraction spectroscopy (X pert PRO, Panalytical with Kα = 1.54056 Å) and micro-Raman spectroscopy (VG Multilab 2000, Thermo VG Scientific, UK).

3. Results and discussion

3.1 Microstructural and structural analysis

The sputtered tungsten oxide thin films were subjected to TEM, AFM, SEAD, and X-ray diffraction studies to assess their microstructural properties and to conduct a qualitative phase analysis. The TEM (Fig. 2a) and AFM (Fig. S1, supporting information) images; indicate that the obtained product had a particle size smaller than 10 nm. The HRTEM analysis was carried out to observe the lattice fringes of the as-prepared WO3 nanoparticles (Fig. 2b); and the lattice distance was measured to be of $d_{002} = 0.38 \pm 0.01$nm, which is close to the bulk WO_3 d_{002} value; and suggests the formation of a monoclinic tungsten oxide phase [42, 43]. The selected area electron diffraction (SAED) pattern exhibits diffuse rings, indicating that the sample has a polycrystalline nature. The diffraction pattern; reveals an inner diffuse ring that is indexed to be a combination of the 002, 020 and 200 planes. [44]. Another diffuse ring (Fig.2(c)) appeared just outside of the inner ring and could be indexed as the collective contribution of the 022, $\bar{2}20$ and 202 planes. The diffraction of

the former and latter three planes is overlaid to produce two different diffuse rings. As shown in the inset of Fig. 2(b), the XRD pattern also shows broadening in the diffraction peaks and a large number of overlapping reflections. [44]. These features can be attributed to the small difference in the inter-planar distances of the respective planes and to the nanocrystalline dimension of the particle. For instance, the first intense peak centered at a $2\theta° = 23.64$ is the peak resulting from the overlap of the 002, 020, and 200 reflections. Another intense peak appears at $2\theta \sim 33.46°$, which is due to the overlap of the 022, $\bar{2}20$, 202 reflections resulting from monoclinic symmetry. The deconvolution (Fig. S2) of the first peak observed at 23.64° reveals individual positions for the three different 002, 020 and 200 reflections. The 2θ position of the 002 reflection was found to be 23.12°, which corresponds to an inter-planar distance $d_{002} = 0.384$nm. Thus, the monoclinic $WO_{3+\delta}$ phase is comprised mostly of corner-linked octahedra (see the inset of Fig. 2(c)), resulting in the 4-membered channels along all crystallographic directions. Figure 2(d) shows a cartoon that visually illustrates the monoclinic phase together with the crystallographic planes in the 002 and 022 orientations. The striking consistence in the XRD Space group P21/n and SAED measurements is that both show two intense peaks and distinct diffuse rings. Furthermore, the inter-planar distance (d_{002} = 0.380nm) from the HRTEM measurement and (002)-indexed reflection peak in the SAED pattern are in good agreement with that obtained from the XRD data ($d_{002} = 0.384$nm, Space group P21/n). Thus, the combined results obtained from the XRD, HRTEM and SAED studies indicate that the tungsten oxide film has a nanogranular structure with a monoclinic phase. Further details of the X-ray diffraction study are provided in the Supporting Information.

X-ray photoelectron spectroscopy (XPS) is used to determine the constituent elements and the corresponding oxidation state. The XPS spectra collected from the $WO_{3+\delta}$ sample confirms the

existence of tungsten (W); oxygen (O) with a small amount of carbon as well. Figure 3 (a-b) shows the W*4f* and O*1s* core level spectra of the as-prepared WO_3 sample. The deconvoluted W*4f* spectrum shows a pair of peaks located at 35.98 and 38.1 eV, which correspond to W$4f_{7/2}$ and W$4f_{5/2}$, respectively, indicating the formation of the W^{+6} oxidation state [45, 46]. The deconvoluted O*1s* spectrum consists of main characteristic peak at about 530.98 eV and shoulder at 531.98, which correspond to the lattice oxygen peak and OH groups (or surface contamination), respectively [45]. The XPS data suggest the presence of W^{+6} oxidation states and a slight widening of the binding energy is presumably due to excess oxygen, which is in consistent with the Rutherford back scattering (RBS) and μ-Raman results shown in Fig. 3(c, d). The oxygen to tungsten (O/W) ratio extracted from the RBS measurement is 3.35, indicating the presence of a large excess of oxygen in the film. The excess oxygen can produce new gap states in WO_3, which results in an increase in the electrical conductivity and electrocatalytic activity [47]. Thus, the abundance of oxygen is expected to improve the donor density and charge transfer in the film [45, 47]. Two characteristic peaks centered at 758 and 949 cm^{-1} appear in the Raman spectrum, and these peaks are respectively associated with the O-W-O and W=O stretching modes vibrations [48, 49]. The breadth of the O-W-O peak reveals that the film has a nanogranular structures, which is consistent with the TEM (Fig.1 (a)) and AFM (Fig. S1) observations.

3.2 Electrochemical supercapacitor performance

Cyclic voltammetry (CV) and charge-discharge measurments are carried out in half-cell configuration to investigate the electrochemical supercapacitor properties of the $WO_{3+\delta}$ nanograin electrode film. Fig. 4 (a) shows CV curves between –0.9 and 0.5 V (vs. SCE) in 1M $LiClO_4$+PC

electrolyte with different scan rates of 10, 20, 50, 80 and 100 mVs^{-1}. During the cathodic scan, the current increases due to the reduction of the W^{+6} state into the W^{+5} state, which results in a film with a dark blue color and simultaneous charging of the electrode [41]. The colored film returns to its original color (transparent) during the anodic scan, which oxidizes the previously reduced metal. The intercalation (reduction reaction) of Li^+ ions causes the electrode to be in a colored, charged state while oxidation results in the electrode becoming transparent (bleached) and discharged. One can clearly determine whether the electrode, is either in its charged or discharged state; by observing the change in color during the charge and discharge cycles. The CV analysis; is used to propose the following insertion/extraction (reduction/oxidation) mechanism for the $WO_{3+\delta}$ nanograin electrode:

$$WO_{3+\delta} + xLi + xe^- \text{ (discharged/bleached)} \quad \leftrightarrow \quad Li_xWO_{3+\delta} \text{ (charged/colored)} \qquad (1)$$

The charge transfer from W^{+6} to W^{+5} oxidation states during the diffusion of Li^+ ions causes the electrode change between charged (colored) and discharged (de-colored) states. At a low scan rate, the Li^+ ions diffuse deeply into the electrode, and at a fast scan rate, ionic diffusion occurs primarily near the nanogranular surface. This makes the CV curves look different (Fig. 4a), and results in differences in the charge storage capacity. The specific capacitance is obtained from the CV curves using the following formula;

$$Cs = \frac{1}{2vm\Delta V}\int IdV \qquad (2)$$

where IdV is the area under the curve, v is the scan rate, m is the mass of the active electrode, and ΔV is the potential window. Fig. 4 (b) shows the specific capacitance (Fg^{-1}) as a function of the scan rate (mVs^{-1}) with a broader potential window of 1.4 V (vs SCE). The capacitive current increases quasi-linearly as the scan rate increases and the specific capacitance decreases in a

similar way (see Fig. 4b), corroborating the good rate capability of the nanograin $WO_{3+\delta}$ electrode film and diffusion-controlled reaction based standard Randles–Sevcik equation [50].

Fig. 4 (c) shows the galvanostatic charge/discharge curves measured at various current densities in 1 M $LiClO_4$+PC electrolyte. The potential window is fixed between –0.9 and 0.5V (Vs SCE). The curvature observed in the galvanostatic charge-discharge curves is indicative of the pseudocapacitive behavior and the existence of Faradaic reactions at the nanogranular surface of the electrode [50, 51]. The discharge curve contains two slopes: one is parallel to the y-axis, representing the voltage change (Ir drop), and the other is related to the capacitive component. The specific capacitance (C_S) is calculated using the following formula: [51]

$$C_S = \frac{I\Delta t}{m\Delta V} \qquad (3)$$

where I is the discharge current, and Δt represents the total discharge time. The nanograin $WO_{3+\delta}$ electrode is cycled at various charge-discharge current densities for 5 cycles to test its rate performance (see Fig. 4d). Within 35 cycles, the charge-discharge rate increases from 1.27 to 12.75 Ag^{-1}, and the specific capacitance decreases gradually from 228 to 82 Fg^{-1}. Subsequently, the applied current is reduced back to 5.0 Ag^{-1}, where 88% of the specific capacitance is recovered at approximately 140 Fg^{-1}. The specific capacitance obtained in this study is more impressive than those in the literature for other tungsten-based electrodes, including WO_{3-x} nano-plates (17.5 Fg^{-1}), [52], graphene nanosheet-tungsten oxide composite (143.6 Fg^{-1}) [53], self-assembled $NiWO_4$ (173 Fg^{-1}) [54] and tungsten oxide nanorods (2.8 $mFcm^{-2}$) [55]. The nanograin tungsten oxide electrode also exhibits both an outstanding reversible capacity and a high-rate long-cycle life performance, due to a combination of the faster Li ion diffusion, improved electrical conduction and robust structure of the material [46, 50, 56].

The long-term electrochemical cycling stability at a high rate is evaluated using both charge/discharge; and CV tests in 1 M $LiClO_4$+PC electrolyte for up to 2000 cycles, as shown in Figs. 5(a) and 5(b), respectively. The specific capacitance and capacitance retention from the charge-discharge curves were obtained at a current density of 12.75 Ag^{-1}. The initial specific capacitance of approximately 90 Fg^{-1} decreases gradually, and after 2000 charge-discharge cycles it decreases down to 67 Fg^{-1} (approximately 75 % of the initial capacitance value). The long-cycled CV curves after the 100^{th} cycle are shown in Fig. S3 (supporting information). The CV curves and the areas under the curves after the initial cycling remain unchanged for up to 2000 cycles. The CVs exhibit reversible characteristics without apparent deviations in each cycle, confirming the good electrochemical stability of the nanogranular tungsten oxide electrode. The capacitance and capacitance retention calculated from the CV curves are shown in Fig. 5(b). The specific capacitance is quite stable after an initial decrease, and high values are maintained over 2000 cycles. The initial quick drop in the specific capacitance is presumably a result of structural changes in the electrode material. Repeated charge-discharge cycles induce the formation of neutral Li-O compounds [57], and once the Li-O layer settles on the electrode surface, the dissolution process becomes less effective and leads to an improvement in the electrochemical stability.

3.3 Electrochromic performance

We now turn to the electrochromic properties of the nonogranular $WO_{3+\delta}$ electrode. The coloring and bleaching performance of the electrode is evaluated using optical transmittance measurements with a potential step of ± 0.75 V (vs. SCE) for a fixed time of 30s. The transmittance modulation in the colored and bleached states is observed in the range from 350 to 800 nm (see

Fig. 6(a)). The transmittance modulation between the colored and bleached states at 630 nm is 82%, which is very impressive when compared to the values of other electrochromic systems, in the literature [9-13]. The change in the optical density (ΔOD) at 630 nm is calculated using the following formula [9]:

$$(\Delta OD)_{630nm} = \ln\left(\frac{T_b}{T_c}\right) \quad (4)$$

where T_b and T_c are the transmittances of the bleached and colored states, respectively. The ΔOD is found to be 2.21. The coloration efficiency (CE), defined as the change in the optical density per unit charge inserted into the electrochromic film, is then calculated using the following equation [3, 10]:

$$CE_{630nm} = \left(\frac{(\Delta OD)_{630nm}}{Q/A}\right) \quad (5)$$

where Q/A is the unit charge density. The charges intercalated during the charging process and de-intercalated during the discharging process is measured using chronocolumetry (see Fig. 6(b)). The obtained CE of ~170 cm^2/C is much higher than what was previously reported for other tungsten oxide-based electrochromic devices [7, 9-13]. The significant improvement in the coloration efficiency is due to the favorable energy levels for charge injection and an increased number of available transitions (quantum mechanical states) from W^{+6} to W^{+5} (Li^+W^{+5} formation) during the Li^+ ion intercalation process [41]. Another possible reason is that structural defects, such as oxygen, act as stable storage sites for Li^+ ion diffusion [51]. The remaining energy level can be easily visualized through a simultaneous change in color with varying voltage. Fig. 6(c) shows photographic images of the nanogranular tungsten oxide electrode in different bleached/colored states at different potentials (colored: –0.25, –0.45, –0.75 V, bleached: +0.75 vs

SCE), which are associated with different amounts of stored charge. The electrode turns dark blue when fully charged at −0.75 V (vs SCE) and becomes transparent in the fully discharged state at +0.75 V (vs SCE). The electrode exhibits a light yellow and light blue color when partially charged at in-between potentials like −0.25 and −0.45 V (vs SCE). The superior coloration efficiency of the nanogranular $WO_{3+\delta}$ electrode makes it possible to efficiently and quantitatively detect the level of charge remaining on the electrode.

We perform ex-situ XPS and AFM measurements after the 1st charge and discharge processes to better understand the Li^+ ion storage mechanism for the tungsten oxide electrode, as shown in Fig. 7 (a-d). The oxidation state of tungsten (W) in the electrode is characterized by recording the ex-situ XPS spectra for tungsten oxide. The XPS spectrum of the tungsten core level (W4*f*) after the charge process (colored state) shows two peaks centered at 35.35 and 37.48 eV, which correspond to $W4f_{7/2}$ and $W4f_{5/2}$ respectively, confirming the formation of the W^{+5} oxidation state [47]. The corresponding AFM (Fig. 7c) image shows a significant change in microscopic morphology, which is presumably caused by the formation of amorphous Li_xWO_3 upon lithiation. On the other hand, the W4*f* XPS spectrum after the discharge process (transparent bleached state) exhibits two similar peaks at higher energies, 35.98 and 38.00 eV, indicating the formation of the W^{+6} oxidation state [45, 46]. The XPS results are consistent with the reaction mechanism in Equation 1. The AFM image (Fig. 7d) shows a microscopic morphology similar to that of the as-prepared tungsten oxide film upon delithiation.

The core level O*1s* XPS spectra taken after the charge and discharge processes shows peaks at 530.48 eV and 530.98 eV, respectively (see Fig. 7(b)). The major peak at 530.48 eV of the W oxidation state and lattice oxygen shifts to a lower energy level than that of the *O1s* spectra of the as-prepared sample at about 0.5 eV after the charge process (Fig.3b) and it regains its original

position after the discharge process. This phenomenon is associated with the Fermi level shift after charging (coloring). The formation of metallic W is further evidenced by recording the Nyquist plots after the charge-discharge processes (Fig. S4). The reduced impedance (Fig. S5a) after the charge process corroborates the conversion of highly-resistive W^{+6} into metallic W^{+5}. Upon discharging, the metallic species becomes oxidized, increasing the impedance (Fig. S4b).

4. Conclusions

In summary, a highly-efficient electrochromic supercapacitor was demonstrated using an oxygen-rich nanogranular tungsten oxide thin film. The excess oxygen plays a critical role in forming a favorable microstructure, such as distorted tunnels along all directions that accommodate the maximum number of Li^+ ions possible. It exhibits faster, reversible color modulation between the blue (charged) and transparent (discharged) states, thereby providing dynamic visual information on the status of the energy storage. The measured properties include a specific capacitance of 228 Fg^{-1} at a current density of 1.27 Ag^{-1}, improved durability without apparent deviations in each cycle over 2000 cycles, and good capacity retention of 75%. In addition, it shows the highest coloration efficiency of ~170 cm^2/C with an optical modulation of 82%. This superior tungsten oxide nanograin electrode material could be used as a safe, efficient, long cycle electrode material for next-generation supercapacitor applications with additional functionality.

Acknowledgements

This project was supported by the National Research Foundation (NRF) of Korea (Grant Nos. 2015M2A2A6A02045252, 2015R1D1A1A01060743, 2015R1D1A1A01058851, 2016R1A6A1A03012877)

Figure captions

Fig. 1. Color palette of electrochromic supercapacitor (smart-supercapacitor) electrodes reported in the literature, together with the coloration efficiency.

Fig. 2. (a,b) TEM and HRTEM images with 10 and 2 nm scale bars respectively. The inset shows the X-ray amorphous nature of the synthesized film. The SAED pattern of the corresponding film is shown in (c), and the inset shows that the monoclinic WO_3 phase is mostly comprised of corner linked octahedra of 4 membered channels along all crystallographic directions. The 002 and 022 crystallographic planes obtained from the SEAD patterns are projected in (d). All crystallographic projections are made with the VESTA structure drawing software.

Fig. 3. Core level XPS spectra showing W*4f* and O*1s* peaks for the synthesized tungsten oxide sample (a, b), indicating the existence of W^{6+} oxidation states; (c) The presence of excess oxygen in the film is confirmed via Rutherford back scattering spectroscopy; (d) The μ-Raman results show broad characteristic Raman peaks centered at 758 cm^{-1} for the nanostructured amorphous tungsten oxide.

Fig. 4.(a) CV curves recorded at 10, 20, 50, 80 and 100 mVs^{-1} scan rates between –0.9 and 0.5 V (vs. SCE) in 1M $LiClO_4$+PC electrolyte, (b) Specific capacitance (Fg^{-1}) and cathodic current (mA) as a function of the scan rate (mVs^{-1}), measured at -0.9 V (vs SCE); (c) Galvanostatic charge/discharge curves recorded at 1.27, 2.54, 5.0, 7.6, and 12.75 Ag^{-1}; (d) Rate performance of the supercapacitive electrode cycled at various charge-discharge current densities for 5 cycles.

Fig. 5.(a) Specific capacity and capacity retention as a function of the cycle number studied at a high current density of 12.75 Ag^{-1}, after 2000 charge-discharge cycles where the capacity is retained up to 75 %, and the associated capacity fading is of 0.0125 % per cycle, (b) Specific capacitance and capacitance retention obtained from CV at 100 mVs^{-1} as a function of the cycle number.

Fig. 6. (a) Transmittance spectra for tungsten oxide in the colored and bleached states at ±0.75 V (vs. SCE) for a fixed time of 30s, with transmittance modulation of 82 %; (b) Chronocolumetry measurements for coloration and bleaching at ±0.75 V; (c) Comparison of the coloration efficiency obtained (~170 cm^2/C) for the previously reported PANI /WO_3 composite and pure WO_3 devices; (d) Actual photographic image of the color scheme at a different potential (–0.25, –0.45, –0.75 V vs SCE) and its bleached state (+0.75 V vs SCE) associated with several typical levels of stored charge.

Fig. 7. Ex-situ XPS, and AFM analysis after the 1stcharge and discharge process (a) Core level W*4f* spectra after the charge and discharge processes, (b) Core level O*1s* spectra after the charge process; (c) Core level O*1s* spectra after the discharge process; (d) The AFM image after the charge (lithiation) process shows a significant change in the microstructure; (e) The AFM image after discharge (delithiation) shows a microstructure similar to that of pristine tungsten oxide.

References

[1] D. Wei, Maik R. J. Scherer, C. Bower, P. Andrew, T. Ryhänen, U. Steiner, Nano Lett. 12 (2012) 1857−1862.

[2] Y. Y Tian, S. Cong, W. M. Su, H. Y. Chen, Q. W. Li, F. X. Geng, Z. G. Zhao, Nano Lett. 14 (2014) 2150–2156.

[3] G. Cai, X. Wang, M. Cui, P. Darmawan, J. Wang, A. Lee-Sie Eh, P. S. Leen, Nano Energy 12 (2015) 258–267.

[4] P. Yang, P. Sun, W. Mai, Mater. Today (2015), http://dx.doi.org/10.1016/j.mattod.2015.11.007

[5] X. L. Chen, H. J. Lin, P. N. Chen, G. Z. Guan, J. Deng, H. S. Peng, Adv. Mater. 26 (2014) 4444–4449.

[6] X.Chen , H. Lin , J. Deng , Y. Zhang , X. Sun , P. Chen , X. Fang , Z. Zhang , G. Guan, H. Peng, Adv. Mater. 26 (2014) 8126–8132.

[7] H. Wei, D. Ding, X. Yan, J. Guo, L. Shao, H. Chen, L. Sun, H. A. Colorado, S. Wei, Z. Guo, Electrochim. Acta 132 (2014) 58 – 66.

[8] H. Wei, X. Yan, S. Wu, Z. Luo, S. Wei, Z. Guo, J. Phys. Chem. C 116 (2012) 25052 – 25064.

[9] G. F. Cai, J. P. Tu, D. Zhou, X. L. Wang, C. D. Gu, Solar Energy Mater. Sol. Cells 124 (2014) 103–110.

[10] F. Lin, C. P. Li, G. Chen, R. C. Tenent, C. A. Wolden, D. T Gillaspie, A. C Dillon, R. M Richards, C. Engtrakul, Nanotechnology 23 (2012) 255601.

[11] A. Subrahmanyam,, A. Karuppasamy, Sol. Energy Mater. Sol. Cells **9**1 (2007) 266-274.

[**12**] A. J.More , R. S. Patil , D. S.Dalavi S. S. Mali , C. K. Hong , M. G. Gang , J. H. Kim, P. S. Patil, Mater. Lett. 134 (2014) 298–301.

[13] D. S. Dalavi, R. S. Devan, R. A. Patil, R. S. Patil, Y. R.Ma, S. B. Sadale, I. Y. Kim, J. H. Kim, P. S. Patil, J. Mater. Chem. C 1 (2013) 3722–3728.

[14] H. Li, Y. Lv, X. Zhang, X. Wang, X. Liu, Solar Energy Mater. Sol. Cells 136 (2015) 86–91.

[15] R. Yu, Z. H. Meng, M. D. Ye, Y. H. Lin, N. B. Lin, X. Y. Liu, W. D. Yu, X. Y. Liu, Cryst. Eng. Comm, 17 (2015) 6583–6590.

[16] R. R. Kharade, S. S. Mali, S. P. Patil, K. R. Patil, M. G. Gang, P. S. Patil , J. H. Kim, P. N. Bhosale, Electrochimica Acta 102 (2013) 358–368.

[17] G. F. Cai, J. P. Tu, D. Zhou, J. H. Zhang, X. L. Wang, C. D. Gu, Solar Energy Mater. Sol. Cells 122 (2014) 51–58.

[18] G. F. Cai, D. Zhou, Q. Q. Xiong, J. H. Zhang, X. L. Wang, C. D. Gu, J. P. Tu, Solar Energy Mater. Sol. Cells 117 (2013) 231–238.

[19] D. Zhou, F. Shi, D. Xie, D. H. Wang, X. H. Xia, X. L. Wang, C. D. Gu, J. P. Tu, J. Colloid Inter. Scie. 465 (2016) 112–120.

[20] A. Karuppasamy, Appl. Surf. Scie. 359 (2015) 841–846.

[21] H. Li, J. Chen, M. Cui, G. Cai, A. L. S. Eh, P. S. Lee, H. Wang, Q. Zhangc, Y. Li, J. Mater. Chem. C 4 (2016) 33-38.

[22] G. Cai, P. Darmawan, M. Cui, J. Chen, X. Wang, A. L. S. Eh, S. Magdassi, P. S. Lee, Nanoscale 8 (2016) 348–357.

[23] I. Sorar, E. Pehlivan, G. A. Niklasson, C. G. Granqvist, Appl. Surf. Sci. 318 (2014) 24–27.

[24] I. Sorar, E. Pehlivan, G. A. Niklasson, C. G. Granqvist, Solar Energy Mater. Sol. Cells 115 (2013) 172–180.

[25] S. Liu, X. Zhang, P. Sun, C. Wang, Y. Wei, Y. Liu, J. Mater. Chem. C 2 (2014) 7891–7896.

[26] N. Usha, R. Sivakumar, C. Sanjeeviraja, Y. Kuroki, J. Alloys Compd. 649 (2015) 112-121.

[27] R. Romero, E.A. Dalchiele, F. Martı´n , D. Leinen, J. R. Ramos-Barrado, Solar Energy Mater. Sol. Cells 93 (2009) 222–229.

[28] S. H. Mujawar, A. I. Inamdar, C. A. Betty, V. Ganesan, P. S. Patil, Electrochimica Acta 52 (2007) 4899–4906.

[29] Y. Liu, C. Jia, Z. Wan, X. Weng, J. Xie, L. Deng, Solar Energy Mater. Sol. Cells 132 (2015) 467–475.

[30] H. S. Shim, V. R. Shinde, H. J. Kim, Y. E. Sung, W. B. Kim, Thin Solid Films 516 (2008) 8573–8578.

[31] V. V. Kondalkar, S. S. Mali, R. R. Kharade, K. V. Khot, P. B. Patil, R. M. Mane, S. Choudhury, P. S. Patil, C. K. Hong, J. H. Kim, P. N. Bhosale, Dalton Trans. 44 (2015) 2788–2800.

[32] D. S. Dalavi, R. S. Devan, R. S. Patil, Y. R. Ma, M. G. Kang, J. H. Kim, P. S. Patil, J. Mater. Chem. A 1 (2013) 1035–1039.

[33] F. Lin, D. T. Gillaspie, A. C. Dillon, R. M. Richards, C. Engtrakul, Thin Solid Films 527 (2013) 26–30.

[34] M. A. Vidales-Hurtado, A. Mendoza-Galván, Solid State Ionics 179 (2008) 2065–2068.

[35] J. Denayer, G. Bister, P. Simonis, P. Colson, A. Maho, P. Aubry, B. Vertruyen, C. Henrist, V. Lardot, F. Cambier, R. Cloots, Appl. Surf. Sci. 321 (2014) 61–69.

[36] Y. F. Yuana, X. H. Xia, J. B. Wu, Y. B. Chen, J. L. Yang, S. Y. Guo, Electrochimica Acta 56 (2011) 1208–1212

[37] F. Cao, G. X. Pan, X. H. Xia, P. S. Tang, H. F. Chen, Electrochimica Acta 111 (2013) 86–91.

[38] X. H. Xia, J. P. Tu, J. Zhang, X. L. Wang, W. K. Zhang, H. Huang, Solar Energy Mater. Sol. Cells 92 (2008) 628–633.

[39] L. D. Kadam, P. S. Patil, Solar Energy Mater. Sol. Cells 69 (2001) 361-369.

[40] A. C. Sonavane, A. I. Inamdar, P. S. Shinde, H. P. Deshmukh, R. S. Patil, P. S. Patil, J. Alloys Compd. 489 (2010) 667–673.

[41] A. I. Inamdar, Y. S. Kim, B. U. Jang, H. Im, W. Jung, D. Y. Kim, H. Kim, Thin Solid Films 520 (2012) 5367–5371.

[42] J. A. Perri, E. Banks, B. Post, J. Appl. Phys. 28 (1957) 1272-1274.

[43] P. M. Woodward, A. W. Sleight, T. Vogt, J. Phys.Chem.Solids 56 (1995) 1305-1315.

[44] B. Hou, D. Parker, G. P. Kissling, J. A. Jones, D. Cherns, D. J. Fermín, J. Phys. Chem. C 117 (2013) 6814−6820.

[45] G. Wang, Y. Ling, H. Wang, X. Yang, C. Wang, J. Z. Zhang, Y. Li, Energy Environ. Sci., 5 (2012) 6180-6187.

[46] J. Li, Y. Liu, Z. Zhu, G. Zhang, T. Zou, Z. Zou, S. Zhang, D. Zeng, C. Xie, Scientific Reports 3, 2409

[47] Y. Wang, T. Zhou, K. Jiang, P. Da, Z. Peng, J. Tang, B. Kong, W. B. Cai, Z. Yang, G. Zheng, Adv. Energy Mater. 4 (2014) 1400696.

[48] J. G. Liu, Y. Zhao, Z. J. Zhang, J. Phys.: Condens. Matter, 15 (2003) L453–L461.

[49] T. Kubo, Y. Nishikitani, J. Electrochem. Soc. 145 (1998) 1729.

[50] A.I. Inamdar, Y. Jo, J. Kim, J. Han, S.M. Pawar, R.S. Kalubarme, C.J. Park, J.P. Hong, Y. S. Park, W. Jung, H. Kim, Hyunsik Im, Energy 83 (2015) 532-538.

[51] Y. Jo, W. J. Cho, A. I. Inamdar, B. C. Kim, J. Kim, H. Kim, H. Im, K. H. Yu, D. Y. Kim, J. Appl. Polym. Sci. 131 (2014) 40306.

[52] S. Lee, Y. W. Lee, D. H. Kwak, M. C. Kim, J. Y. Lee, D. M. Kim, K. W. Park, Ceramics International 41 (2015) 4989–4995.

[53] Y. Caia, Y. Wanga, S. Denga, G. Chena, Q. Lia, B. Hana, R. Hana, Y. Wang, Ceramics International 40 (2014) 4109–4116.

[54] U. Nithiyanantham, S. Rao Ede, S. Anantharaj, S. Kundu Cryst. Growth Des. 15 (2015) 673-686.

[55] S. H. Park,, Y. H. Kim, T. G. Lee, H. K. Shon, H. M. Park, J. Y. Song, Mater. Res. Bull. 47 (2012) 3612−3618.

[56] P. Poizot , S. Laruelle , S. Grugeon , L. Dupont , J. M. Tarascon , Nature 407 (2000) 496-499 .

[57] J. H. Ku, J. H. Ryu, S. H. Kim, O. H. Han, S. M. Oh, Adv. Funct. Mater. 22 (2012) 3658–3664.